CHEMISTRY OF MATERIALS

Article

pubs.acs.org/cm

In Situ Chemical Imaging of Solid-Electrolyte Interphase Layer Evolution in Li−S Batteries

Manjula I. Nandasiri,[∥,†] Luis E. Camacho-Forero,[‡] Ashleigh M. Schwarz,[∥] Vaithiyalingam Shutthanandan,[∥] Suntharampillai Thevuthasan,[∥] Perla B. Balbuena,[‡] Karl T. Mueller,[∥,§] and Vijayakumar Murugesan*[,∥,§]

[∥]Pacific Northwest National Laboratory, Richland, Washington 99354, United States

[‡]Department of Chemical Engineering, Texas A&M University, College Station, Texas 77843, United States

[§]Joint Center for Energy Storage Research (JCESR), Pacific Northwest National Laboratory, Richland, Washington 99354, United States

Supporting Information

ABSTRACT: Parasitic reactions of electrolyte and polysulfide with the Li-anode in lithium sulfur (Li−S) batteries lead to the formation of solid-electrolyte interphase (SEI) layers, which are the major reason behind severe capacity fading in these systems. Despite numerous studies, the evolution mechanism of the SEI layer and specific roles of polysulfides and other electrolyte components are still unclear. We report an in situ X-ray photoelectron spectroscopy (XPS) and chemical imaging analysis combined with ab initio molecular dynamics (AIMD) computational modeling to gain fundamental understanding regarding the evolution of SEI layers on Li-anodes within Li−S batteries. A multimodal approach involving AIMD modeling and in situ XPS characterization uniquely reveals the chemical identity and distribution of active participants in parasitic reactions as well as the SEI layer evolution mechanism. The SEI layer evolution has three major stages: the formation of a primary composite mixture phase involving stable lithium compounds (Li_2S, LiF, Li_2O, etc.) and formation of a secondary matrix type phase due to cross interaction between reaction products and electrolyte components, which is followed by a highly dynamic monoanionic polysulfide (i.e., LiS_5) fouling process. These new molecular-level insights into the SEI layer evolution on Li-anodes are crucial for delineating effective strategies for the development of Li−S batteries.

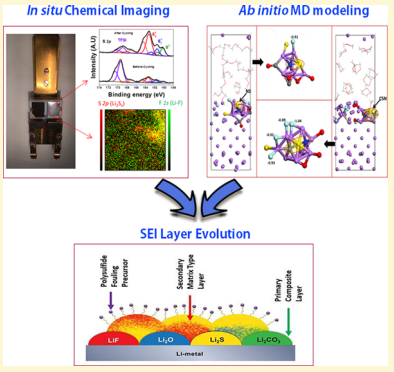

INTRODUCTION

The lithium−sulfur (Li−S) battery is a promising candidate for next generation energy storage due to its high theoretical specific capacity (1675 mA.h.g^{-1}) and up to 5-fold increase in energy density (2567 W·h·kg^{1-}) as compared to state-of-the-art lithium-ion batteries (LIBs).[1−5] However, there are critical challenges to overcome to realize the commercialization of Li−S batteries (LSBs). One of the most demanding challenges is effectively protecting the Li-metal anode from parasitic reactions that cause insulating solid-electrolyte interphase (SEI) layer formation, which seriously limits the capacity retention and life cycles.[6−9] Parasitic chemistry at the Li-metal anode is typically a combination of redox, decomposition, substitution, and coordination reactions depending on the choice of electrochemistry and electrolyte materials. For example, in the Li−S electrochemical system, the elemental sulfur cathode (S_8) is reduced to Li_2S through multiple intermediate lithium polysulfide species (Li_2S_x; $x \leq 8$) during the discharge process.[3] The longer chain lithium polysulfide species (Li_2S_x; $x \geq 6$) are highly soluble in electrolyte solvents and can diffuse to the Li-anode, causing complex redox and/or complexation reactions. Although molecular level details of polysulfide reactions with Li-metal are still unknown, it is hypothesized that polysulfides reduce to insoluble Li_2S and Li_2S_2 species with subsequent SEI layer formation.[10,11] In addition to the polysulfides, highly reactive transient species arising from decomposition of electrolyte components (such as solvents and counteranions) can also be part of parasitic chemical reactions leading to subsequent SEI layer evolution.[12,13] This parasitic chemistry involving many complex reactions and transient molecules creates the chemically and topographically inhomogeneous SEI layer on the active Li-anode surfaces. Such a sporadic fouling process can increase the interfacial resistance for Li^+ ion diffusion due to the thick deposits of insulating and insoluble species on Li-anodes.[2] In order to limit the complex parasitic reactions at Li-anodes and improve the performance of LSBs, it is important to unravel the mechanisms of parasitic chemistry and subsequent SEI layer formation. In particular, gaining a real time perspective of the SEI layer evolution is both critical and extremely challenging, as many of its constituents and originating reactions are transient and highly air-sensitive in nature.[14] Few experimental

Received: January 27, 2017
Revised: May 1, 2017
Published: May 3, 2017

DOI: 10.1021/acs.chemmater.7b00374
Chem. Mater. 2017, 29, 4728−4737

techniques are capable of probing the SEI layer formation, and ab initio based computational modeling was recognized as an efficient and convenient tool for analyzing the SEI layer formation.[15−18]

Despite the technical challenges in building in situ spectroscopic and microscopic capabilities for the analysis of LSBs, some efforts were made in recent years to capture the evolution and dynamic changes in the SEI layer during battery cycling.[14,19−21] Nevertheless, none of the spectroscopic studies could capture the entire reaction suite and identify all constituents associated with SEI layer formation in LSBs. For example, element specific spectroscopic techniques such as nuclear magnetic resonance (NMR), electron paramagnetic resonance (EPR), and X-ray absorption spectroscopy (XAS) were able to provide only a fractional view of complex parasitic reactions by monitoring a single reactant and/or products.[20,22−28] Similarly, the in situ microscopic techniques such as transmission X-ray microscopy (TXM)[29,30] and X-ray fluorescence microscopy[31] were employed to understand the spatial evolution of SEI layers but lack the critical chemical speciation. Despite various in situ efforts, the gap in knowledge that would provide a comprehensive understanding of SEI layer evolution at the Li-metal anode in LSBs remains and inhibits the design and formulation of optimal electrolytes.[32] To gain a comprehensive and molecular-level view of the parasitic reactions and subsequent SEI layer evolution, we have developed a first-of-its-kind in situ X-ray photoelectron spectroscopy (XPS) capability that can simultaneously provide spatially resolved chemical imaging as well as chemical speciation through high resolution core-level spectroscopy of critical elements. By combining in situ XPS results with ab initio molecular dynamics (AIMD) computational modeling, molecular level insight is realized regarding the distinct roles of transient species from parasitic reactions and the subsequent SEI layer evolution during cycling processes of LSBs.

EXPERIMENTAL DETAILS

The high vapor pressures of elemental sulfur (S_8) and aprotic electrolyte solvents such as 1,3-dioxolane (DOL) and dimethoxyethane (DME) are the central challenge in developing in situ XPS for Li−S batteries. To overcome this issue, we employed an ultrahigh vacuum (UHV) compatible ionic liquid (IL), 1-butyl-1-methylpyrrolidinium bis(trifloromethylsulfonyl)imide, i.e., $[bmpyr]^+[TFSI]^-$, as a cosolvent in the electrolyte. The $[bmpyr]^+$ $[TFSI]^-$ ionic liquid used in this study has been reported as a compatible electrolyte for Li−S cells due to their high electrochemical stability.[33−35] Various ionic liquids have also been used as electrolytes and are electrochemically stable in the voltage range (±2.2 V) of Li−S batteries.[36,37] A solution of 1 M Li_2S_6 dissolved in a DOL and DME solvent mixture is prepared as reported earlier[38] (see the Supporting Information). Subsequently, 20 wt % of the Li_2S_6 in DOL and DME solution is mixed with $[bmpyr]^+$ $[TFSI]^-$ and used as the final electrolyte system for the in situ study (see the Supporting Information). Apart from the vacuum compatibility, the specific choice of $[TFSI]^-$ counteranion containing IL is to ensure the electrolyte system represents the traditional Li−TFSI salt widely used in the Li−S battery studies. In addition, this electrolyte solution resembles the typical Li−S battery after the discharge cycle, where the lithium polysulfide (Li_2S_x) species are expected to get dissolved in DOL/DME solvent. In this case, however, the volatile sulfur cathode is replaced with graphite foil and Li_2S_6 dissolved in the electrolyte solvent mixture is used as a sulfur source by initiating the redox process via the charging cycle. A schematic of the in situ XPS sample holder is shown in Figure 1. The Li-anode and graphite-cathode materials can be mounted on a Teflon base and subsequently connected with gold wires as an external electrical contact line to the electrochemical analyzer. The reservoir in between

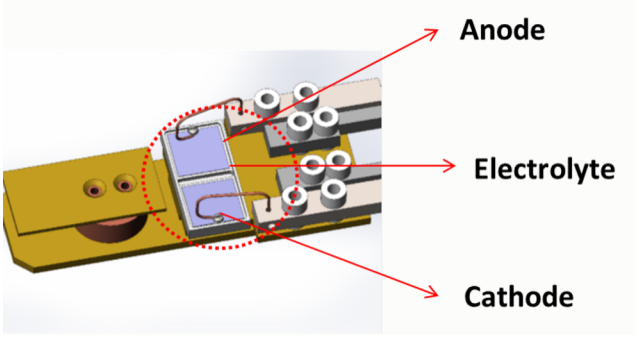

Figure 1. Schematic diagram of the XPS sample holder developed for battery cycling and in situ XPS characterization.

the anode and cathode is filled with an electrolyte mixture such that it covers half of the electrode surfaces. The cell is fully charged and discharged at 2.2 V for two consecutive cycles only due to the limited availability of active sulfur material. All measurements are performed on the Li-electrolyte interfacial region at the end of each charge/discharge cycle to avoid the charge-induced XPS peak shifts (see the Supporting Information). The graphite cathode is fully covered by ionic liquid due to high surface wetting processes (see the Supporting Information).

XPS analysis was performed using a Kratos Axis Ultra DLD spectrometer, which consists of a high performance Al Kα monochromatic X-ray source (1486.6 eV) and a high resolution hemispherical mirror analyzer. The X-ray source was operated at 150 W, and emitted photoelectrons were collected at the analyzer entrance slit normal to sample surface. The data acquisition was carried out in a hybrid mode with an analysis area of 700 × 300 μm. The survey spectra were recorded at a pass energy of 160 eV with 0.5 eV step size, and high resolution spectra were recorded at a pass energy of 20 eV with step size of 0.1 eV. The pass energy of 20 eV in the 700 × 300 μm analysis area is referenced to the fwhm of 0.59 eV for Ag $3d_{5/2}$. A charge neutralizer with low energy electrons was used to exclude surface charging effects, and the binding energy of C 1s at 284.8 eV was used as the charge reference. The elemental and chemical state maps were acquired using the imaging XPS capability in the Kratos Axis Ultra system. The maps were collected in a field of view of 800 μm with a spatial resolution of ∼5 μm. The imaging XPS data were collected under a pass energy of 160 eV at each peak and background energy. The chamber pressure was maintained at $\lesssim 5 \times 10^{-9}$ Torr during all measurements. XPS data were analyzed using the CasaXPS software assuming Gaussian/Lorentzian (30% Lorentzian) line shapes and utilizing Shirley background correction. All the XPS binding energies reported here have an uncertainty of ±0.1 eV. The background subtraction and imaging data processing were accomplished using the CasaXPS software to obtain the elemental and chemical state XPS maps presented here.

Reaction energies for possible decomposition reactions of Li_2S_6 at the Li-anode were calculated using Density Functional Theory (DFT) as implemented in the Gaussian 09 package[39] with a hybrid functional B3PW91 and the 6-311+G(3df,p) basis set. The polarizable continuum model (PCM)[40] was used for describing the DME solvation effects. After polysulfide and salt decompositions take place, several SEI products are formed. The analyses of these complexes (typically of the form: X-Li-species-Li-X) were performed on the basis of the resulting products after 20 ps of AIMD simulation of electrolyte mixtures consisting of 1 M LiTFSI in DOL/DME in contact with a Li metal surface as described in our previous study.[41] The Li-metal anode was modeled as a (100) Li crystallographic plane. In addition to the salt and solvent, the electrolyte also contained a 1 M Li_2S_8 polysulfide species. Although the polysulfide used in these simulations is a longer chain than that used in the experiments, it is expected to yield almost the same final SEI components by the end of the decomposition process. The AIMD simulations were performed using the Vienna ab Initio Simulation Package (VASP).[42,43] All the AIMD calculations

DOI: 10.1021/acs.chemmater.7b00374
Chem. Mater. 2017, 29, 4728−4737

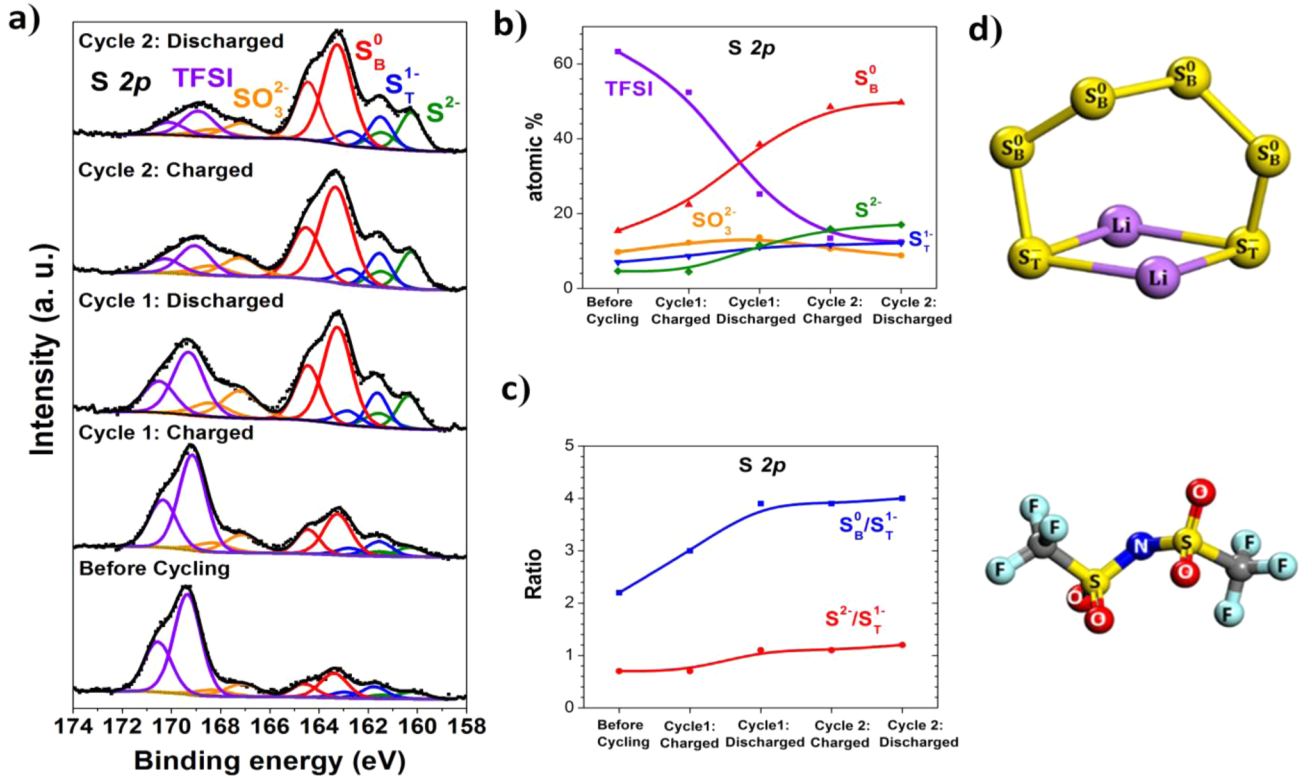

Figure 2. (a) Core level S 2p XPS spectra of the Li-electrolyte interfacial region with subsequent charge/discharge cycles. (b) Evolution of various sulfur based species over charge/discharge cycles based on atomic concentration derived from S 2p peak areas. (c) The ratio between terminal sulfide and bridging sulfur atoms (S_B^0/S_T^{1-}) along with the disulfide and sulfide ratio (S^{2-}/S^{1-}) derived from S 2p peak areas. (d) Molecular structure of lithium polysulfide Li_2S_6 (top) and TFSI anion (bottom) with chemical labels used in the XPS analysis.

were based on DFT within the Perdew–Burke–Ernzerhof generalized gradient approximation (GGA-PBE).[44] Although the electron transfer rates may be significantly underestimated using semilocal generalized gradient approximation functionals, the AIMD results provide good insights into the decomposition pathways and identification of products. The projector augmented wave (PAW) pseudopotentials[45,46] were used. The energy cutoff of the plane-wave basis expansion was set to 400 eV. A NVT ensemble at 330 K was used with a time step of 1 fs and a Nose thermostat (see our previous study[41] for more details). Finally, the electronic charges were calculated by using the Bader charge analysis.[47−49]

RESULTS AND DISCUSSION

In situ XPS and imaging XPS were carried out at the interfacial region between Li metal anode and IL/Li_2S_6 electrolyte before and after the charge/discharge process (see the Supporting Information). The high resolution S 2p core level XPS spectra of Li metal anode before cycling and after each charge/discharge cycle are shown in Figure 2. The S 2p spectra is a doublet comprised of closely spaced spin–orbit components (ΔE = 1.16 eV; intensity ratio = 0.511) arising from $2p_{3/2}$ and $2p_{1/2}$. Each sulfur compound shows the characteristic doublet, and only the high intensity $2p_{3/2}$ will be discussed hereafter for simplicity (see the Supporting Information). The sulfone group (R–SO_2–R) of the TFSI anion is observed at 169 eV along with broad sulfide peaks encompassing the 160–165 eV binding energy regime.[50,51] In addition, a low intensity peak at 167.2 eV representing sulfite (SO_3^{2-}) or thiosulfate ($S_2O_3^{2-}$) species is also observed.[52,53] Deconvolution of S 2p spectra under the broad sulfide region gave three unique components, namely, sulfide dianion (S^{2-}) of Li_2S at 160.2 eV along with terminal sulfur (S_T^{1-}) and bridging sulfur (S_B^0) of lithium polysulfide (Li_2S_x with $x > 1$) at 161.6 and 163.3 eV, respectively.[52,54] On the basis of the evolution of different sulfide concentrations (Figure 2b and Table S1) during the cycling process, we can analyze the polysulfide shuttling process and subsequent parasitic reaction with the Li-anode, which is widely believed to be a major cause for capacity loss in LSBs batteries. Similarly, the S 2p peak ratio between the bridging and terminal sulfur, i.e., S_B^0/S_T^{1-} of the polysulfide species, can be used as a qualitative indicator of polysulfide speciation (see the Supporting Information).

Before cycling, the polysulfide components (S_T^{1-} and S_B^0) are about 22 at. % of total sulfur and the S_B^0/S_T^{1-} ratio is about 2.2 in accordance with our starting electrolyte mixture, which is predominantly Li_2S_6 (Figure 2d). After the first charge cycle, the total amount of polysulfide components increased to ∼30 at. % whereas the lithium sulfide (S^{2-}) concentration remains unchanged (5 at. % of total sulfur). During the charging process, Li^+ cations move toward the Li-anode and engage in the Li-plating process ($Li^+ + e^- \rightarrow Li^0$). Such an electrochemically driven process includes the Li^+ cations, which are part of lithium polysulfide species, and initiates the polysulfide shuttling process. A significant increase in polysulfide components after the charging cycle clearly indicates that the polysulfide shuttling process mainly depends on the Li–S interaction strength relative to Li–solvent and Li–TFSI interactions. Such a Li^+ driven shuttling process will lead to accumulation of polysulfide species and starts the fouling process at the Li-anode, which is followed through increased concentrations of polysulfide components in the XPS spectra after a charge cycle. Interestingly, the S_B^0/S_T^{1-} ratio increases to ∼3 indicating that the parent Li_2S_6 polysulfide species evolves

DOI: 10.1021/acs.chemmater.7b00374
Chem. Mater. 2017, 29, 4728−4737

into other types of polysulfide species during the fouling process, which will be discussed later.

During the discharge process, the Li-anode undergoes Li-stripping processes releasing Li^+ and electrons, which can reduce the accumulated long chain polysulfides to lithium sulfide (S^{2-}). Evidently, the lithium sulfide (S^{2-}) concentration is nearly doubled (~10 at. %) after the first discharge cycle and further increases to 15 at. % of the total sulfur concentration during the second charge and discharge cycles. The significant increase in S^{2-} concentration during the discharge cycles indicates that the longer chain polysulfides accumulated at the Li-anode are being reduced to insoluble Li_2S and subsequently become irreversible parts of the SEI layer during the first discharge cycle.[55] This Li_2S formation covers the Li-anode surface and restricts further sulfide reduction during subsequent cycling processes as noted by the similar S^{2-} concentrations in the second charge and discharge cycles. Interestingly, the total amount of polysulfide components (S_T^{1-} and S_B^0) increases further to ~50 at. % and eventually reaches a plateau value of ~63 at. % during the second charge/discharge cycles (see Figure 2b). It is expected that the polysulfide will shuttle back toward the cathode side during the discharge process based on the Li^+ flow direction. However, we observed continuous increases in polysulfide and Li_2S concentration at the Li-anode leading to loss of active materials (i.e., scarcity of polysulfide solute in IL electrolyte) and subsequently causing cell failure and preventing further cycling studies. This finding indicates that the fouling process is mostly irreversible and the polysulfide is chemically interacting with the other components of the SEI layer. We postulate that various components of SEI layers can strongly interact with polysulfide solutes in the electrolyte and cause continuous fouling processes that are supported by the increase in polysulfide concentration during the cycling process (see Figure 2b). This observation is in agreement with a previous AIMD analysis, which predicted the clustering of polysulfide chains near the Li_2S layer as part of SEI formation.[11] Nevertheless, the cluster formation is favored for lower order polysulfide chains (Li_2S_x with $x < 6$), which would require lower S_B^0/S_T^{1-} ratios (≤2).[38] In addition, recent reports suggest the formation of insoluble Li_2S_2 from polysulfide reduction processes at the Li-anode.[56] The observed increase in terminal polysulfide (S_T^{1-}) peak intensity with cycling initially seems to support the presence of Li_2S_2 species within the SEI layer (see Figure 2b). However, any such Li_2S_2 formation should significantly decrease the S_B^0/S_T^{1-} and S^{2-}/S_T^{1-} ratios. Conversely, we observed that these ratios increase with charge/discharge cycles (see Figure 2c), which strongly suggests that Li_2S_2 is not the dominant sulfide phase in the SEI layer.

Interestingly, the S_B^0/S_T^{1-} ratio of ~4 is even higher than the possible longer polysulfide chain (i.e., Li_2S_8 for which S_B^0/S_T^{1-} ratio is 3). Therefore, an increase in S_B^0/S_T^{-1} ratio could result from two possible scenarios: (a) the relative concentration of terminal sulfur within the polysulfide decreasing possibly due to parasitic redox reactions; (b) the presence of a new form of sulfur species which has the same binding energy (~163.5 eV) and overlaps with the S_B^0 peak. Our previous studies of sulfur cathode materials have revealed that both pristine elemental sulfur (S_8) and carbon bonded sulfur (with C−S^0 bonds) can also register S 2p peaks at the same binding energy (~163.5 eV) as of the bridging sulfur (S_B^0) of the polysulfides.[57] Theoretical studies have predicted the formation of elemental sulfur (S_8) as a product of dissociation of polysulfide anions (see Li−S batteries),[55] via the reaction

$$S_8^{2-} \rightarrow 2S_3^{-} + (1/4)S_8 \quad \Delta G_{Soln}^{298K} = -0.17\,eV \tag{1}$$

Nevertheless, our recent AIMD simulations predicted that longer polysulfide chains are reduced very rapidly near the Li-anode.[11,41] Thus, it is very unlikely to detect formation of neutral S_8 on the bare surface of the Li-metal electrode. Hence, we carried out new DFT simulations to provide more insight into the possible decomposition of the precursor Li_2S_6. The calculated Gibbs free energy in DME solvent reveals two possible reduction processes,

$$Li_2S_6 + 2Li^0 \rightarrow Li_2S + Li_2S_5 \quad \Delta G_{Soln}^{298K} = -4.69\,eV \tag{2}$$

$$Li_2S_6 + Li^0 \rightarrow Li_2S + LiS_5 \quad \Delta G_{Soln}^{298K} = -1.29\,eV \tag{3}$$

Our DFT results indicate that the reduction product of Li_2S_5 is energetically favorable (eq 2) but represents a S_B^0/S_T^{1-} ratio of 1.5. Despite its favorable formation energy (ΔG_{soln}), the Li_2S_5 formation requires a higher concentration of Li^0 (i.e., prevalent access to Li-metal surface) relative to the LiS_5 formation process. This implies that, with restricted access to Li-metal, the reduction product of LiS_5 would be more probable (see eqs 2 and 3). Formation of LiS_5 (S_B^0/S_T^{1-} = 4) can account for the simultaneous increase of both Li_2S concentration and S_B^0/S_T^{1-} ratio (~3.9) observed in the in situ XPS results (see Figure 2c). Such a reduction process can occur at the terminal sulfur atom of the polysulfide molecule (i.e., S_T^{1-} to S^{2-}), which will result in a significant increase in the S_B^0/S_T^{1-} ratio and S^{2-} concentration, agreeing with our observations (see Figure 2c). However, the long-term stability of LiS_5 molecule within the SEI layer still needs to be evaluated further with other analytical techniques.

In addition to the polysulfide shuttling, the SEI layer formation would also depend on the TFSI anion decomposition process. The decomposition of TFSI anion can be simultaneously monitored by the evolution of sulfone and sulfite peaks observed in the higher binding energy regime (>166 eV) in the S 2p spectra (see Figure 2a). Before cycling, the sulfone peak from TFSI species represents ~63 at. % of total sulfur concentration on the Li-anode. During the first charge and discharge cycles, the amount of sulfone species drops to ~53 and 27 at. %, respectively. Subsequently, after the second charge and discharge cycles, it drops to about 20 at. %, relative to sulfide and polysulfide concentrations (see Figure 2c). Such a significant drop in the pristine TFSI anion concentration on the Li-anode indicates two possible mechanisms: (a) a set of redox reactions altering the sulfone group as part of TFSI decomposition; (b) displacement of some TFSI molecules by polysulfide species at the Li-anode surface due to the SEI layer formation process within the XPS analysis volume. Recently, Cui and co-workers suggested that the sulfone group of TFSI anion can undergo oxidation processes at the Li-anode and produce sulfite (SO_3^{2-}) and sulfate (SO_4^{2-}) species based on XPS analysis.[56] However, they did not considered the sulfur spin−orbit based doublet in their peak deconvolution, and the reported (SO_4^{2-}) species peak (~170 eV) falls within the S $2p_{1/2}$ component of the sulfone group of a pristine TFSI molecule. Our results do not show the presence of any sulfate but only the sulfite (SO_3^{2-}) species, which shows minimal changes during the cycling process (~4 at. %) and fails to account for the significant drop in pristine TFSI concentration (see Figure 2c). Decomposition of the sulfone group and formation of $Li_2S_2O_4$ and Li_2SO_3 were proposed in the literature, and this mechanism can explain the

DOI: 10.1021/acs.chemmater.7b00374
Chem. Mater. 2017, 29, 4728−4737

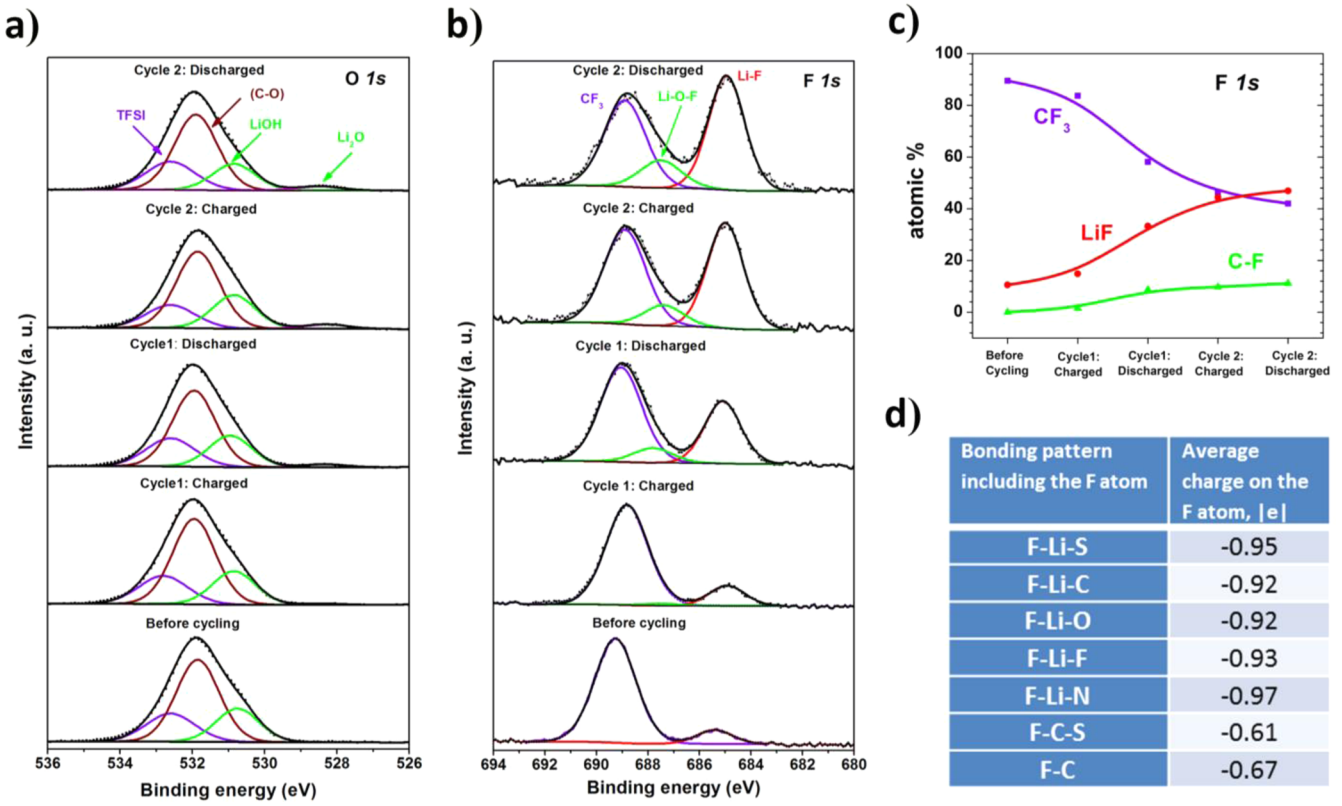

Bonding pattern including the F atom	Average charge on the F atom, |e|
F-Li-S	-0.95
F-Li-C	-0.92
F-Li-O	-0.92
F-Li-F	-0.93
F-Li-N	-0.97
F-C-S	-0.61
F-C	-0.67

Figure 3. (a) Core level O 1s XPS spectra of the Li-electrolyte interfacial region with subsequent charge/discharge cycles. (b) Core level F 1s XPS spectra of Li-electrolyte interfacial region with charge/discharge cycles. (c) Evolution of various fluorine based species over charge/discharge cycles based on atomic concentration derived from respective F 1s peak areas. (d) The various fluoride based species from TFSI decomposition predicted from AIMD calculations along with their respective electronic charges.

low intensity sulfite peak (~10 at. %) observed at ~167 eV during the cycling process.[58,59] The other possibility would be the reduction of the sulfone group of the TFSI molecule to sulfur (S^0), which will fall in the sulfide regime of the XPS spectra and thereby increase the S_B^0 concentration as observed in a higher S_B^0/S_T^{1-} ratio. However, unless the sulfone group of a TFSI anion undergoes multielectron reduction (from S^{6+} to S^0) at the Li-metal anode, the decomposed products are expected to be at higher binding energy (>166 eV) similar to the sulfite/thiosulfate or sulfone regions. Since multielectron reduction is less likely, we do not expect a significant increase in S^0 due to this mechanism. The second scenario would be displacement of TFSI anions by the polysulfide fouling process discussed earlier. Typically, the TFSI anion can interact with the counterion from the IL (i.e., $[bmpyr]^+$), Li-anode, and Li^+ from the polysulfide species. During the cycling process, we observed that the polysulfide reduces to insoluble Li_2S, which can grow as a passivating film on the Li-anode surface.[11,41] Such a Li_2S passivation layer can inhibit the Li^+-TFSI^- interactions and enhance the $[bmpyr]^+-TFSI^-$ ion pairing. However, it should be noted that the Li_2S passivation layer is unlikely to be uniform and the TFSI anion will compete for interactions with the exposed Li-anode surfaces (vide infra) and cause the TFSI decomposition process. The TFSI anion decomposition is a cascade process with many transient species including sulfone and fluoride groups, which can subsequently interact with lithium polysulfide molecules and the Li-anode.[41] This process supports our previous discussion regarding the polysulfide species interacting with other components of the SEI layer and causing continuous fouling processes on the Li-anode. This clustering process will be further justified a posteriori below using other elemental analysis.

The TFSI anion decomposition process at the Li-anode can be followed through O 1s and F 1s spectra for deeper understanding of the SEI layer formation. The O 1s spectra is dominated by a broad peak centered around 532 eV, which can be assigned to C−O bonds within DOL/DME (electrolyte solvents) as well as lithium carbonate (Li-metal surface impurity) owing to their small chemical shift differences (see Figure 3a).[58,60] Deconvolution of the broad O 1s spectra revealed shoulder peaks at ~532.6 and 530.6 eV indicating the S−O bonds (sulfone and sulfite) and lithium hydroxide (Li-metal surface impurity), respectively.[60] There is no significant change in the concentration of these oxygen species during the cycling process. We also observe a low intensity (~3 at. %) peak at 528.5 eV with the cycling process indicating lithium oxide (Li_2O) formation at the Li-anode as a result of TFSI decomposition. Although, the decomposition of the sulfone group can cause Li_2O formation,[41] the presence of carbonate and hydroxide native impurities at the Li-anode surface (see Figure S4) can also lead to lithium oxide. The main product of TFSI decomposition would be lithium fluoride (LiF) formation from C−F bond breaking at the Li-anode.[41] Such a decomposition process can be analyzed through F 1s spectra (see Figure 3b). The F 1s spectra show a dominant TFSI anion peak (CF_3) at 688.8 eV along with a low intensity Li−F related species peak around 685 eV.[50,58,60] The Li−F related species formation even before the cycling process demonstrates the instability of TFSI anions on the Li-metal anode. The concentration of Li−F species is about 11 at. % of total

DOI: 10.1021/acs.chemmater.7b00374
Chem. Mater. 2017, 29, 4728−4737

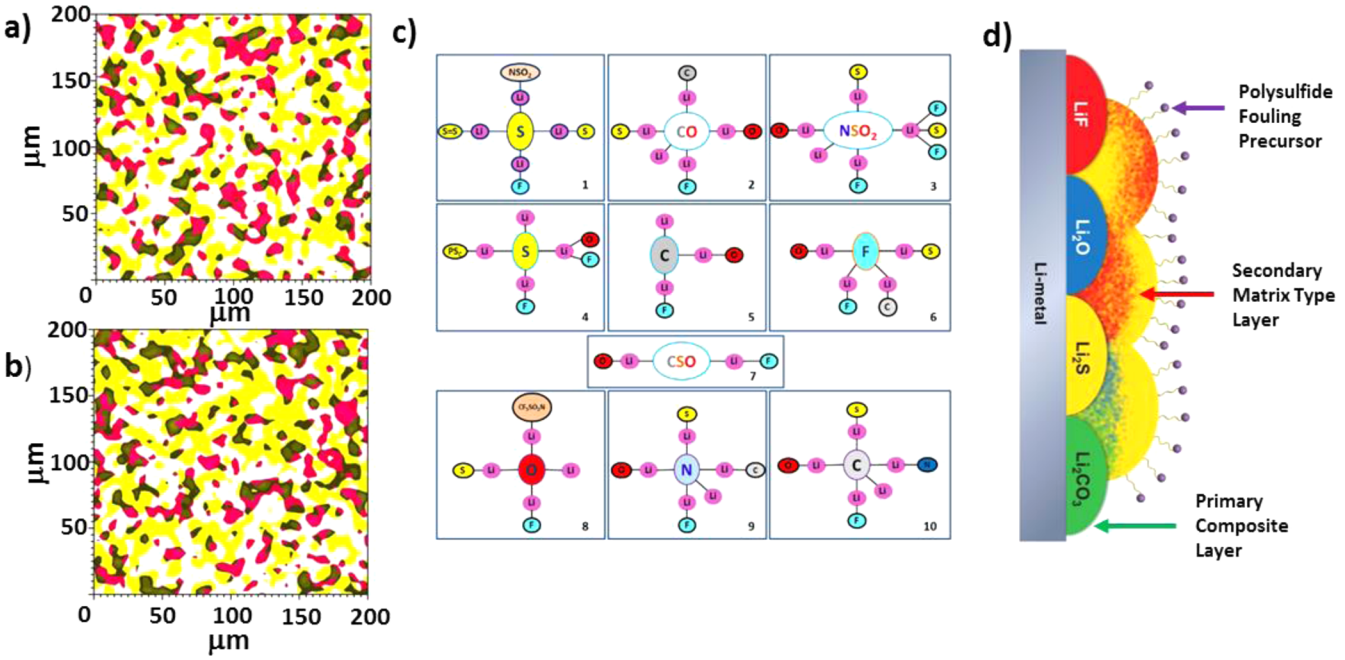

Figure 4. XPS chemical imaging of the Li-electrolyte interfacial region after (a) first charging cycle and (b) first discharging cycle. The Li−F species from F 1s spectra and S^0 polysulfide species from S 2p spectra are represented as yellow and red regions, respectively. The black region represents the overlapping regions of Li−F and S^0polysulfide species. (c) Schematic representation of various fluorine based Li−F species predicted from AIMD calculations. (d) Cartoon representation of SEI layer growth mechanism based on the combined XPS and computational results (see text for details).

fluorine before cycling and increases to 15 at. % following the first charging cycle (see Table S2). During the subsequent discharge cycle, the amount of this Li−F based species more than doubles to ∼33 at. % (see Figure 3c). Such a substantial increase in the amount of Li−F species must correlate to accelerated decomposition of the TFSI anion during the discharge process. This peak at ∼685 eV in the F 1s spectra is widely reported as evidence of LiF formation.[61−64] In addition, a new shoulder peak (∼687.5 eV) arises near the parent CF_3 peak following the charge/discharge process, which is traditionally assigned to C−F intermediate species as part of TFSI decomposition.[41,65] However, such a simplified peak assignment can hinder deeper understanding of the SEI layer evolution. To clearly identify the possible fluoride species within the SEI layer, we analyzed various components of TFSI decomposition products predicted by our previous AIMD simulations[41] (see Figures S5−S7). Since the charge state of an atomic site dictates the binding energy of XPS spectra, we analyzed the average electronic charges of the F atom for various decomposition products and relevant fluoride atomic arrangements along with their average charge as shown in Figure 3d. These fluorine containing species generally fall in two categories based on the charge at the F atom. The first category is fluorine directly bonding to Li where the F atom takes the highest negative charge (ionic bonding), and the second is fluorine directly bonding with C atoms in which a much lower negative charge is observed (covalent bonding). The F−C−S bond (when part of an otherwise pristine TFSI molecule) holds the lowest charge (−0.61 eV) and is expected produce a signal at high binding energy (688.8 eV) in the F 1s spectra. The C−F bonding interaction, which may correspond to the different intermediates (radical and anions) formed during the TFSI decomposition such as CF, CF_2, and CF_3, holds slightly elevated charge (−0.67 eV) at the F atom and is observed as a shoulder peak at ∼688 eV. However, it should be noted that the CF_3^- remaining intact after the C−S bond cleavage during TFSI decomposition has a longer life span and is more likely to represent the shoulder peak observed under cycling conditions.[41] Similarly, the lower binding energy (∼685 eV) peak represents various species involving Li−F ionic bonding, such as F−Li−S, F−Li−O, and the traditional LiF phase. At the end of the initial charge cycle, the C−F species remains at very low concentration (∼1 at. %) relative to total fluorine concentration but increases to 9 at. % following the first discharge cycle. This suggests further decomposition of TFSI anion at the fully discharged state, which is typically initiated by C−S bond cleavage and subsequent breaking of the CF_3 bond to C−F and F^- species and the formation of Li−F related species.[41] The decomposition of TFSI anion continued during the second charging cycle resulting in 33% and 11% increases in Li−F and C−F species, respectively, relative to the fully discharged anode. However, both Li−F and C−F species reached a plateau after the second discharge cycle, which resembles the saturation of the polysulfide fouling process (see Figure 2b). A similar trend observed for both TFSI decomposition and the polysulfide fouling process in the SEI layer evolution supports our previous deduction that the polysulfide molecules interact with various components of the SEI layer including the TFSI decomposition products. Our previous in situ NMR and AIMD computational analysis have unveiled the presence of sulfide based transient radicals and reactive fluoride anions at the Li-anode participating in the SEI layer formation process.[28,41] During the cycling process, the redox based parasitic reactions can cause highly reactive transient species (such as sulfide radicals and fluoride anions) that can initiate clustering of nearby electrolyte components through polymerization and subsequently leads to precipitation-induced SEI layer formation on the Li-anode.[66] Although the high resolution in situ XPS analysis revealed the evolution of polysulfide and Li−F species as the major components, the

DOI: 10.1021/acs.chemmater.7b00374
Chem. Mater. 2017, 29, 4728−4737

growth mechanism of SEI layer formation is still elusive, mainly due to extreme complexity involving parasitic reaction rate, Li-anode surface chemistry, and the concentration gradient of solutes. In particular, the concentration gradient of solutes at the interfacial regime can dictate the composition of the cluster and subsequent SEI layer nucleation and growth phenomena.[67]

We also employed XPS spectromicroscopy to analyze the underlying growth mechanism of the SEI layer, which can provide realistic views of concentration gradients in the spatial domain.[68,69] Figure 4 shows a two-dimensional chemical imaging performed at the same spot on the Li-anode after the first charge/discharge process (see the Supporting Information). The interfacial region (800 × 800 μm) is scanned at 685 eV (F 1s; Li−F species) and 163.3 eV (S 2p; S_B^0) binding energies to monitor the TFSI anion and polysulfide gradient with a spatial resolution of about 5 μm. The contour mapping of chemical imaging clearly shows the clustering of reactive solutes, polysulfide (blue) and Li−F related species (red), within the top layers of the anode−electrolyte interfacial region, which can subsequently precipitate as an SEI layer (Figure 4a,b). Since the XPS imaging is typically dominated by the concentration gradient of the top layer (<5 nm) within the interfacial regime, the delimited white background represents SEI layers adjacent to the Li-anode surface with relatively lower concentration of polysulfide and LiF. It should be noted that the discharge cycle has a higher concentration of polysulfide and Li−F species than that during the charge cycle. The rise in polysulfide concentration after the discharge cycle simply reflects the expected polysulfide shuttling toward the Li-anode. Such clustering of polysulfide at the interfacial region can facilitate Li_2S precipitation as a SEI layer due to possible reduction reactions (see eqs 2 and 3). Similarly, the clustering of Li−F species can cause precipitation of lithium fluoride (LiF) phases within the SEI layer. The presence of well separated clusters of polysulfide (blue) and Li−F (red) represents the nucleation seeds for Li_2S and LiF phases and evolves as a dominant part of SEI layer evolution. Intriguingly, the total Li−F species increases along with polysulfide from the shuttling process during the discharge cycle, indicating that the F^- anion from TFSI decomposition interacts with lithium polysulfide (see Figure.4b). The overlapped signal (black) in the imaging map indicates a possible cross-interaction between F^- anion and lithium polysulfides. This corroborates our a priori assumption that the reactive transient species involving polysulfide and fluoride anion can chemically interact and initiate clustering with various electrolyte components. For example, AIMD computational results predicted multiple types of Li−F species involving various electrolyte components (see Figure 4c and the Supporting Information), which could also be part of clustering phenomena that can initiate the precipitation as part of the SEI layer.

Combining high resolution XPS and chemical imaging analysis with AIMD computational modeling results, we can begin unravelling the SEI layer growth mechanism. The SEI layer is commonly viewed as a multiphase material with chemically distinctive phases (such as LiF, Li_2S, Li_2O, and Li_2CO_3) separated by well-defined boundaries[16] (see Figure 4c). In fact, clearly distinguishable clustering of polysulfide (blue) and Li−F (red) species supports this multiphase structural view of the SEI layer. However, significant overlapping of polysulfide and Li−F regions (black) reveals the presence of a matrix type SEI layer with continuous phases and diffuse boundaries between the various sulfide and fluoride based regimes (see Figure 4d). The simultaneous multiphase and continuous phase SEI layer formation can be explained by the Stranski−Krastanov (SK) growth model developed for thin film nucleation processes.[67] On the basis of this growth model, the SEI layer formation can be viewed as a two-step process where (a) the products of parasitic reactions at the Li-anode surface result in multiphase layers (such as Li_2S, Li_2O, and LiF) and (b) clustering of transient species from parasitic reactions, by strongly interacting with the electrolyte and other SEI components, leads to a matrix type precipitation. During the evolution of the first step, the parasitic products need to be adjacent to the Li-anode surface to gain expedited access to preferably unbound Li^+ ions that can facilitate an extended network of Li_2S and LiF solid multiphase layers. For example, clustering of polysulfide as part of the shuttling process on the Li-anode can cause the nucleation of Li_2S phases by accessing the Li stripping process during discharge cycles. With growth to critical thickness, this insoluble multiphase layer can significantly inhibit the access to unbound Li^+ from the Li-anode and thereby activate the second stage of the SEI layer growth. With restricted access to the Li-metal surface and scarcity of unbound Li^+ ions, the parasitic reaction products will react with each other as well as with adjacent electrolyte components to initiate nucleation directly on the multiphase layer and produce a matrix type phase with diffused boundaries. In particular, the restricted access to Li-metal can cause partial polysulfide reduction processes (eq 3) leading to a monoanionic polysulfide (LiS_5) as a major component of the secondary layer that results in a high S_B^0/S_T^{1-} ratio (≥3). This secondary SEI layer mainly consists of aggregated polysulfides and oligomeric reactive products and is comparable to the organic phase layer comprised of polymerized solvents reported in lithium-ion batteries.[13,59,66] Nevertheless, the major difference is that it involves polysulfides as a main component and also serves as absorbent layer for the shuttling polysulfides, which leads to an exponential increase in polysulfides after the first charge/discharge cycle in high resolution in situ XPS (see Figure 2b). In addition, the adsorbed polysulfides can undergo association and disproportionation reactions causing oligomeric aggregates on top of the SEI layer, which are evident from the clustering of polysulfides detected via in situ imaging XPS analysis (see Figure 4b).[38] Unlike the primary multiphase layer containing inorganic solid phases, the constituents of the second stage matrix type layer could be relatively soluble and hence subsequent polysulfide fouling will be a dynamic process depending on electrolyte composition and cycling current rate. In short, the oligomeric aggregation of polysulfides on the SEI layer entraps the active material on the Li-anode and manifests as the severe capacity fading that is widely reported in the Li−S battery literature. To this end, our study suggests that effective Li-metal protection requires careful design of protective scaffolds, which not only prevent the inorganic multiphase primary layer but also inhibit the polysulfide fouling process.

CONCLUSIONS

In summary, in situ XPS and computational modeling studies were carried out on a model Li−S battery system to understand the growth mechanism of the SEI layer on the Li-anode. The XPS core level spectra of S 2p showed a gradual increase of sulfide dianion (S^{2-}) indicating the formation of insoluble and electronically insulating Li_2S due to polysulfide reduction processes. Similarly, the F 1s spectra showed a significant

DOI: 10.1021/acs.chemmater.7b00374
Chem. Mater. 2017, 29, 4728−4737

increase in Li−F and C−F species with a decrease in CF_3 (associated with pristine TFSI anion) indicating its decomposition in the proximity of the Li-anode. Evolution of both Li_2S and Li−F species with cycling causes the precipitation of an inorganic multiphase layer as the primary SEI component. A simultaneous exponential increase of polysulfide species (S^0 and S^{1-}) suggests a continuous fouling process on the Li-anode during both charge and discharge cycles. The high S_B^0/S_T^{1-} ratio (>3) observed for the polysulfide species involved in this fouling process indicates the formation of monoanionic polysulfide (i.e., LiS_5) due to restricted access to Li-metal during the sulfide reduction process. With access to the Li-metal surface becoming restricted, the parasitic reaction products (fluoride and sulfide anions) will engage in cross-interaction with adjacent electrolyte components and nucleate into a secondary matrix type SEI layer, which is visualized as clustering in XPS imaging and supported by AIMD analysis. The continuous increase in polysulfide concentration at the Li-anode interface also suggests a facilitated fouling process due to its absorption on a matrix type SEI layer. Chemical entrapment of the dissolved polysulfides at the top of the matrix type layer on the Li-anode causes the fouling and subsequent continuous loss of active material, leading to the severe capacity fading widely observed in Li−S battery technologies. Ultimately, controlling the role of SEI layer in Li−S batteries will require a multifunctional scaffold design, which can deflect the shuttling polysulfide as well as inhibit the electrolyte decomposition on Li-anode surfaces.

■ ASSOCIATED CONTENT

Supporting Information

The Supporting Information is available free of charge on the ACS Publications website at DOI: 10.1021/acs.chemmater.7b00374.

Detailed experimental procedures on synthesis of Li_2S_6 electrolyte, in situ XPS cell design and analysis, and DFT and AIMD simulation studies (PDF)

■ AUTHOR INFORMATION

Corresponding Author

*E-mail: vijay@pnnl.gov. Tel: (509)-371-6540 (V.M.).

ORCID

Perla B. Balbuena: 0000-0002-2358-3910

Karl T. Mueller: 0000-0001-9609-9516

Vijayakumar Murugesan: 0000-0001-6149-1702

Present Address

†M.I.N.: Department of Physics, Montana State University, Bozeman, MT 59717.

Author Contributions

The manuscript was written through contributions of all authors. M.I.N., A.M.S., S.T., and V.S. conducted the in situ XPS analysis. L.E.C.-F. and P.B.B. carried out the DFT and AIMD simulation studies. V.M. and K.T.M. designed and supervised the project.

Notes

The authors declare no competing financial interest.

■ ACKNOWLEDGMENTS

The in situ XPS cell designs were funded by the Chemical Imaging Initiative as part of the Laboratory Directed Research and Development (LDRD) program at Pacific Northwest National Laboratory (PNNL). The Li−S battery materials and measurements were funded through the Joint Center for Energy Storage Research (JCESR) sponsored by Department of Energy Basic Energy Science (DOE-BES) program. The in situ XPS characterization was carried out in the Environmental Molecular Sciences Laboratory (EMSL), a DOE Office of Science User Facility sponsored by the Office of Biological and Environmental Research and located at PNNL. L.E.C.-F. and P.B.B. acknowledge financial support from the Assistant Secretary for Energy Efficiency and Renewable Energy, Office of Vehicle Technologies of the U.S. Department of Energy under Contract No. DE-EE0006832 under the Advanced Battery Materials Research (BMR) Program. Supercomputer resources from Texas A&M University High Performance Computer Center and Texas Advanced Computing Center (TACC) are gratefully acknowledged. V.M. and P.B.B. thank Dr. Nav Nidhi Rajput, LBNL, for fruitful discussions regarding computational modeling results.

■ REFERENCES

(1) Barghamadi, M.; Kapoor, A.; Wen, C. A Review on Li-S Batteries as a High Efficiency Rechargeable Lithium Battery. *J. Electrochem. Soc.* **2013**, *160*, A1256−A1263.

(2) Bruce, P. G.; Freunberger, S. A.; Hardwick, L. J.; Tarascon, J.-M. Li-O2 and Li-S batteries with high energy storage. *Nat. Mater.* **2012**, *11*, 19−29.

(3) Ji, X.; Nazar, L. F. Advances in Li-S batteries. *J. Mater. Chem.* **2010**, *20*, 9821−9826.

(4) Lin, Z.; Liang, C. Lithium-sulfur batteries: from liquid to solid cells. *J. Mater. Chem. A* **2015**, *3*, 936−958.

(5) Yin, Y.-X.; Xin, S.; Guo, Y.-G.; Wan, L.-J. Lithium−Sulfur Batteries: Electrochemistry, Materials, and Prospects. *Angew. Chem., Int. Ed.* **2013**, *52*, 13186−13200.

(6) Budi, A.; Basile, A.; Opletal, G.; Hollenkamp, A. F.; Best, A. S.; Rees, R. J.; Bhatt, A. I.; O'Mullane, A. P.; Russo, S. P. Study of the Initial Stage of Solid Electrolyte Interphase Formation upon Chemical Reaction of Lithium Metal and N-Methyl-N-Propyl-Pyrrolidinium-Bis(Fluorosulfonyl)Imide. *J. Phys. Chem. C* **2012**, *116*, 19789−19797.

(7) Markevich, E.; Salitra, G.; Rosenman, A.; Talyosef, Y.; Chesneau, F.; Aurbach, D. The effect of a solid electrolyte interphase on the mechanism of operation of lithium-sulfur batteries. *J. Mater. Chem. A* **2015**, *3*, 19873−19883.

(8) Cheon, S.-E.; Choi, S.-S.; Han, J.-S.; Choi, Y.-S.; Jung, B.-H.; Lim, H. S. Capacity Fading Mechanisms on Cycling a High-Capacity Secondary Sulfur Cathode. *J. Electrochem. Soc.* **2004**, *151*, A2067−A2073.

(9) Diao, Y.; Xie, K.; Xiong, S.; Hong, X. Insights into Li-S Battery Cathode Capacity Fading Mechanisms: Irreversible Oxidation of Active Mass during Cycling. *J. Electrochem. Soc.* **2012**, *159*, A1816−A1821.

(10) Barchasz, C.; Molton, F.; Duboc, C.; Leprêtre, J.-C.; Patoux, S.; Alloin, F. Lithium/Sulfur Cell Discharge Mechanism: An Original Approach for Intermediate Species Identification. *Anal. Chem.* **2012**, *84*, 3973−3980.

(11) Liu, Z.; Bertolini, S.; Balbuena, P. B.; Mukherjee, P. P. Li2S Film Formation on Lithium Anode Surface of Li−S batteries. *ACS Appl. Mater. Interfaces* **2016**, *8*, 4700−4708.

(12) Li, Y.; Leung, K.; Qi, Y. Computational Exploration of the Li-Electrode|Electrolyte Interface in the Presence of a Nanometer Thick Solid-Electrolyte Interphase Layer. *Acc. Chem. Res.* **2016**, *49*, 2363−2370.

(13) An, S. J.; Li, J.; Daniel, C.; Mohanty, D.; Nagpure, S.; Wood, D. L., III The state of understanding of the lithium-ion-battery graphite solid electrolyte interphase (SEI) and its relationship to formation cycling. *Carbon* **2016**, *105*, 52−76.

(14) Gauthier, M.; Carney, T. J.; Grimaud, A.; Giordano, L.; Pour, N.; Chang, H.-H.; Fenning, D. P.; Lux, S. F.; Paschos, O.; Bauer, C.;

DOI: 10.1021/acs.chemmater.7b00374
Chem. Mater. 2017, 29, 4728−4737

Maglia, F.; Lupart, S.; Lamp, P.; Shao-Horn, Y. Electrode−Electrolyte Interface in Li-Ion Batteries: Current Understanding and New Insights. *J. Phys. Chem. Lett.* **2015**, *6*, 4653−4672.
(15) Ganesh, P.; Kent, P. R. C.; Jiang, D.-e. Solid−Electrolyte Interphase Formation and Electrolyte Reduction at Li-Ion Battery Graphite Anodes: Insights from First-Principles Molecular Dynamics. *J. Phys. Chem. C* **2012**, *116*, 24476−24481.
(16) Leung, K.; Soto, F.; Hankins, K.; Balbuena, P. B.; Harrison, K. L. Stability of Solid Electrolyte Interphase Components on Lithium Metal and Reactive Anode Material Surfaces. *J. Phys. Chem. C* **2016**, *120*, 6302−6313.
(17) Ebadi, M.; Brandell, D.; Araujo, C. M. Electrolyte decomposition on Li-metal surfaces from first-principles theory. *J. Chem. Phys.* **2016**, *145*, 204701.
(18) Chen, X.; Hou, T.-Z.; Li, B.; Yan, C.; Zhu, L.; Guan, C.; Cheng, X.-B.; Peng, H.-J.; Huang, J.-Q.; Zhang, Q. Towards stable lithium-sulfur batteries: Mechanistic insights into electrolyte decomposition on lithium metal anode. *Energy Storage Materials* **2017**, DOI: 10.1016/j.ensm.2017.01.003.
(19) Harks, P. P. R. M. L.; Mulder, F. M.; Notten, P. H. L. In situ methods for Li-ion battery research: A review of recent developments. *J. Power Sources* **2015**, *288*, 92−105.
(20) Hagen, M.; Schiffels, P.; Hammer, M.; Dörfler, S.; Tübke, J.; Hoffmann, M. J.; Althues, H.; Kaskel, S. In-Situ Raman Investigation of Polysulfide Formation in Li-S Cells. *J. Electrochem. Soc.* **2013**, *160*, A1205−A1214.
(21) Patel, M. U. M.; Demir-Cakan, R.; Morcrette, M.; Tarascon, J.-M.; Gaberscek, M.; Dominko, R. Li-S Battery Analyzed by UV/Vis in Operando Mode. *ChemSusChem* **2013**, *6*, 1177−1181.
(22) Wang, Q.; Zheng, J.; Walter, E.; Pan, H.; Lv, D.; Zuo, P.; Chen, H.; Deng, Z. D.; Liaw, B. Y.; Yu, X.; Yang, X.; Zhang, J.-G.; Liu, J.; Xiao, J. Direct Observation of Sulfur Radicals as Reaction Media in Lithium Sulfur Batteries. *J. Electrochem. Soc.* **2015**, *162*, A474−A478.
(23) Cuisinier, M.; Cabelguen, P.-E.; Evers, S.; He, G.; Kolbeck, M.; Garsuch, A.; Bolin, T.; Balasubramanian, M.; Nazar, L. F. Sulfur Speciation in Li−S Batteries Determined by Operando X-ray Absorption Spectroscopy. *J. Phys. Chem. Lett.* **2013**, *4*, 3227−3232.
(24) Lowe, M. A.; Gao, J.; Abruna, H. D. Mechanistic insights into operational lithium-sulfur batteries by in situ X-ray diffraction and absorption spectroscopy. *RSC Adv.* **2014**, *4*, 18347−18353.
(25) Patel, M. U. M.; Arčon, I.; Aquilanti, G.; Stievano, L.; Mali, G.; Dominko, R. X-ray Absorption Near-Edge Structure and Nuclear Magnetic Resonance Study of the Lithium−Sulfur Battery and its Components. *ChemPhysChem* **2014**, *15*, 894−904.
(26) Wujcik, K. H.; Pascal, T. A.; Pemmaraju, C. D.; Devaux, D.; Stolte, W. C.; Balsara, N. P.; Prendergast, D. Characterization of Polysulfide Radicals Present in an Ether-Based Electrolyte of a Lithium−Sulfur Battery During Initial Discharge Using In Situ X-Ray Absorption Spectroscopy Experiments and First-Principles Calculations. *Adv. Energy Mater.* **2015**, *5*, 1500285.
(27) See, K. A.; Leskes, M.; Griffin, J. M.; Britto, S.; Matthews, P. D.; Emly, A.; Van der Ven, A.; Wright, D. S.; Morris, A. J.; Grey, C. P.; Seshadri, R. Ab Initio Structure Search and in Situ 7Li NMR Studies of Discharge Products in the Li−S Battery System. *J. Am. Chem. Soc.* **2014**, *136*, 16368−16377.
(28) Xiao, J.; Hu, J. Z.; Chen, H.; Vijayakumar, M.; Zheng, J.; Pan, H.; Walter, E. D.; Hu, M.; Deng, X.; Feng, J.; Liaw, B. Y.; Gu, M.; Deng, Z. D.; Lu, D.; Xu, S.; Wang, C.; Liu, J. Following the Transient Reactions in Lithium−Sulfur Batteries Using an In Situ Nuclear Magnetic Resonance Technique. *Nano Lett.* **2015**, *15*, 3309−3316.
(29) Lin, C.-N.; Chen, W.-C.; Song, Y.-F.; Wang, C.-C.; Tsai, L.-D.; Wu, N.-L. Understanding dynamics of polysulfide dissolution and redeposition in working lithium−sulfur battery by in-operando transmission X-ray microscopy. *J. Power Sources* **2014**, *263*, 98−103.
(30) Nelson, J.; Misra, S.; Yang, Y.; Jackson, A.; Liu, Y.; Wang, H.; Dai, H.; Andrews, J. C.; Cui, Y.; Toney, M. F. In Operando X-ray Diffraction and Transmission X-ray Microscopy of Lithium Sulfur Batteries. *J. Am. Chem. Soc.* **2012**, *134*, 6337−6343.
(31) Yu, X.; Pan, H.; Zhou, Y.; Northrup, P.; Xiao, J.; Bak, S.; Liu, M.; Nam, K.-W.; Qu, D.; Liu, J.; Wu, T.; Yang, X.-Q. Direct Observation of the Redistribution of Sulfur and Polysufides in Li−S Batteries During the First Cycle by In Situ X-Ray Fluorescence Microscopy. *Adv. Energy Mater.* **2015**, *5*, 1500072.
(32) Lin, D.; Liu, Y.; Cui, Y. Reviving the lithium metal anode for high-energy batteries. *Nat. Nanotechnol.* **2017**, *12*, 194−206.
(33) Barghamadi, M.; Best, A. S.; Bhatt, A. I.; Hollenkamp, A. F.; Mahon, P. J.; Musameh, M.; Rüther, T. Effect of Anion on Behaviour of Li-S Battery Electrolyte Solutions Based on N-Methyl-N-Butyl-Pyrrolidinium Ionic Liquids. *Electrochim. Acta* **2015**, *180*, 636−644.
(34) Vranes, M.; Dozic, S.; Djeric, V.; Gadzuric, S. Physicochemical Characterization of 1-Butyl-3-methylimidazolium and 1-Butyl-1-methylpyrrolidinium Bis(trifluoromethylsulfonyl)imide. *J. Chem. Eng. Data* **2012**, *57*, 1072−1077.
(35) Zheng, J.; Gu, M.; Chen, H.; Meduri, P.; Engelhard, M. H.; Zhang, J.-G.; Liu, J.; Xiao, J. Ionic liquid-enhanced solid state electrolyte interface (SEI) for lithium-sulfur batteries. *J. Mater. Chem. A* **2013**, *1*, 8464−8470.
(36) Höfft, O.; Krischok, S. Vacuum Electrochemistry in Ionic Liquids. *Electrochem. Soc. Interface* **2014**, *23*, 53.
(37) Paulechka, Y. U.; Zaitsau, D. H.; Kabo, G. J.; Strechan, A. A. Vapor pressure and thermal stability of ionic liquid 1-butyl-3-methylimidazolium Bis(trifluoromethylsulfonyl)amide. *Thermochim. Acta* **2005**, *439*, 158−160.
(38) Vijayakumar, M.; Govind, N.; Walter, E.; Burton, S. D.; Shukla, A.; Devaraj, A.; Xiao, J.; Liu, J.; Wang, C.; Karim, A.; Thevuthasan, S. Molecular structure and stability of dissolved lithium polysulfide species. *Phys. Chem. Chem. Phys.* **2014**, *16*, 10923−10932.
(39) Frisch, M. J.; Trucks, G. W.; Schlegel, H. B.; Scuseria, G. E.; Robb, M. A.; Cheeseman, J. R.; Scalmani, G.; Barone, V.; Mennucci, B.; Petersson, G. A.; Nakatsuji, H.; Caricato, M.; Li, X.; Hratchian, H. P.; Izmaylov, A. F.; Bloino, J.; Zheng, G.; Sonnenberg, J. L.; Hada, M.; Ehara, M.; Toyota, K.; Fukuda, R.; Hasegawa, J.; Ishida, M.; Nakajima, T.; Honda, Y.; Kitao, O.; Nakai, H.; Vreven, T.; Montgomery, J. A., Jr.; Peralta, J. E.; Ogliaro, F. O.; Bearpark, M. J.; Heyd, J.; Brothers, E. N.; Kudin, K. N.; Staroverov, V. N.; Kobayashi, R.; Normand, J.; Raghavachari, K.; Rendell, A. P.; Burant, J. C.; Iyengar, S. S.; Tomasi, J.; Cossi, M.; Rega, N.; Millam, N. J.; Klene, M.; Knox, J. E.; Cross, J. B.; Bakken, V.; Adamo, C.; Jaramillo, J.; Gomperts, R.; Stratmann, R. E.; Yazyev, O.; Austin, A. J.; Cammi, R.; Pomelli, C.; Ochterski, J. W.; Martin, R. L.; Morokuma, K.; Zakrzewski, V. G.; Voth, G. A.; Salvador, P.; Dannenberg, J. J.; Dapprich, S.; Daniels, A. D.; Farkas, Ã. d. n.; Foresman, J. B.; Ortiz, J. V.; Cioslowski, J.; Fox, D. J. *Gaussian 09*; Gaussian, Inc.: Wallingford, CT, USA, 2009.
(40) Tomasi, J.; Mennucci, B.; Cammi, R. Quantum Mechanical Continuum Solvation Models. *Chem. Rev.* **2005**, *105*, 2999−3094.
(41) Camacho-Forero, L. E.; Smith, T. W.; Bertolini, S.; Balbuena, P. B. Reactivity at the Lithium−Metal Anode Surface of Lithium−Sulfur Batteries. *J. Phys. Chem. C* **2015**, *119*, 26828−26839.
(42) Kresse, G.; Furthmuller, J. Efficiency of ab-initio total energy calculations for metals and semiconductors using a plane-wave basis set. *Comput. Mater. Sci.* **1996**, *6* (1), 15−50.
(43) Kresse, G.; Hafner, J. Ab initio molecular dynamics for liquid metals. *Phys. Rev. B: Condens. Matter Mater. Phys.* **1993**, *47*, 558−561.
(44) Perdew, J. P.; Burke, K.; Ernzerhof, M. Generalized Gradient Approximation Made Simple. *Phys. Rev. Lett.* **1996**, *77*, 3865−3868.
(45) Blöchl, P. E. Projector augmented-wave method. *Phys. Rev. B: Condens. Matter Mater. Phys.* **1994**, *50*, 17953−17979.
(46) Kresse, G.; Joubert, D. From ultrasoft pseudopotentials to the projector augmented-wave method. *Phys. Rev. B: Condens. Matter Mater. Phys.* **1999**, *59*, 1758−1775.
(47) Tang, W.; Sanville, E.; Henkelman, G. A grid-based Bader analysis algorithm without lattice bias. *J. Phys.: Condens. Matter* **2009**, *21*, 084204.
(48) Sanville, E.; Kenny, S. D.; Smith, R.; Henkelman, G. Improved grid-based algorithm for Bader charge allocation. *J. Comput. Chem.* **2007**, *28*, 899−908.

DOI: 10.1021/acs.chemmater.7b00374
Chem. Mater. 2017, 29, 4728−4737

(49) Henkelman, G.; Arnaldsson, A.; Jónsson, H. A fast and robust algorithm for Bader decomposition of charge density. *Comput. Mater. Sci.* **2006**, *36* (3), 354−360.
(50) Men, S.; Lovelock, K. R. J.; Licence, P. X-ray photoelectron spectroscopy of pyrrolidinium-based ionic liquids: cation-anion interactions and a comparison to imidazolium-based analogues. *Phys. Chem. Chem. Phys.* **2011**, *13* (33), 15244−15255.
(51) Smart, R. S. C.; Skinner, W. M.; Gerson, A. R. XPS of sulphide mineral surfaces: metal-deficient, polysulphides, defects and elemental sulphur. *Surf. Interface Anal.* **1999**, *28* (1), 101−105.
(52) Liang, X.; Hart, C.; Pang, Q.; Garsuch, A.; Weiss, T.; Nazar, L. F. A highly efficient polysulfide mediator for lithium−sulfur batteries. *Nat. Commun.* **2015**, *6*, 5682.
(53) Turner, N. H.; Murday, J. S.; Ramaker, D. E. Quantitative determination of surface composition of sulfur bearing anion mixtures by Auger electron spectroscopy. *Anal. Chem.* **1980**, *52*, 84−92.
(54) Fantauzzi, M.; Elsener, B.; Atzei, D.; Rigoldi, A.; Rossi, A. Exploiting XPS for the identification of sulfides and polysulfides. *RSC Adv.* **2015**, *5*, 75953−75963.
(55) Assary, R. S.; Curtiss, L. A.; Moore, J. S. Toward a Molecular Understanding of Energetics in Li−S Batteries Using Nonaqueous Electrolytes: A High-Level Quantum Chemical Study. *J. Phys. Chem. C* **2014**, *118*, 11545−11558.
(56) Li, W.; Yao, H.; Yan, K.; Zheng, G.; Liang, Z.; Chiang, Y.-M.; Cui, Y. The synergetic effect of lithium polysulfide and lithium nitrate to prevent lithium dendrite growth. *Nat. Commun.* **2015**, *6*, 7436.
(57) Bhattacharya, P.; Nandasiri, M. I.; Lv, D.; Schwarz, A. M.; Darsell, J. T.; Henderson, W. A.; Tomalia, D. A.; Liu, J.; Zhang, J.-G.; Xiao, J. Polyamidoamine dendrimer-based binders for high-loading lithium−sulfur battery cathodes. *Nano Energy* **2016**, *19*, 176−186.
(58) Howlett, P. C.; Brack, N.; Hollenkamp, A. F.; Forsyth, M.; MacFarlane, D. R. Characterization of the Lithium Surface in N-Methyl-N-alkylpyrrolidinium Bis(trifluoromethanesulfonyl)amide Room-Temperature Ionic Liquid Electrolytes. *J. Electrochem. Soc.* **2006**, *153*, A595−A606.
(59) Cheng, X.-B.; Zhang, R.; Zhao, C.-Z.; Wei, F.; Zhang, J.-G.; Zhang, Q. A Review of Solid Electrolyte Interphases on Lithium Metal Anode. *Adv. Sci.* **2016**, *3* (3), 1500213.
(60) Xu, C.; Sun, B.; Gustafsson, T.; Edstrom, K.; Brandell, D.; Hahlin, M. Interface layer formation in solid polymer electrolyte lithium batteries: an XPS study. *J. Mater. Chem. A* **2014**, *2* (20), 7256−7264.
(61) Chan, C. K.; Ruffo, R.; Hong, S. S.; Cui, Y. Surface chemistry and morphology of the solid electrolyte interphase on silicon nanowire lithium-ion battery anodes. *J. Power Sources* **2009**, *189* (2), 1132−1140.
(62) Schroder, K. W.; Celio, H.; Webb, L. J.; Stevenson, K. J. Examining Solid Electrolyte Interphase Formation on Crystalline Silicon Electrodes: Influence of Electrochemical Preparation and Ambient Exposure Conditions. *J. Phys. Chem. C* **2012**, *116*, 19737−19747.
(63) Leroy, S.; Martinez, H.; Dedryvère, R.; Lemordant, D.; Gonbeau, D. Influence of the lithium salt nature over the surface film formation on a graphite electrode in Li-ion batteries: An XPS study. *Appl. Surf. Sci.* **2007**, *253*, 4895−4905.
(64) Song, J.; Noh, H.; Lee, H.; Lee, J.-N.; Lee, D. J.; Lee, Y.; Kim, C. H.; Lee, Y. M.; Park, J.-K.; Kim, H.-T. Polysulfide rejection layer from alpha-lipoic acid for high performance lithium-sulfur battery. *J. Mater. Chem. A* **2015**, *3*, 323−330.
(65) Nguyen, C. C.; Woo, S.-W.; Song, S.-W. Understanding the Interfacial Processes at Silicon−Copper Electrodes in Ionic Liquid Battery Electrolyte. *J. Phys. Chem. C* **2012**, *116* (28), 14764−14771.
(66) Soto, F. A.; Ma, Y.; Martinez de la Hoz, J. M.; Seminario, J. M.; Balbuena, P. B. Formation and Growth Mechanisms of Solid-Electrolyte Interphase Layers in Rechargeable Batteries. *Chem. Mater.* **2015**, *27*, 7990−8000.
(67) Venables, J. A.; Spiller, G. D. T.; Hanbucken, M. Nucleation and growth of thin films. *Rep. Prog. Phys.* **1984**, *47*, 399.
(68) Gurker, N.; Ebel, M. F.; Ebel, H.; Mantler, M.; Hedrich, H.; Schön, P. Imaging XPS—a new technique. 2—Experimental verification. *Surf. Interface Anal.* **1987**, *10*, 242−249.
(69) Gurker, N.; Ebel, M. F.; Ebel, H. Imaging XPS—A new technique, I—principles. *Surf. Interface Anal.* **1983**, *5*, 13−19.

DOI: 10.1021/acs.chemmater.7b00374
Chem. Mater. 2017, 29, 4728−4737